Supporting Information

for

Multi-mode Time-resolved Superresolution Microscopy Revealing Chain Packing and Anisotropic Single Carrier Transport in Conjugated Polymer Nanowires

Yifei Jiang*[‡], Haobin Chen[‡§], Xiaoju Men[£], Zezhou Sun[§], Zhen Yuan[£], Xuanjun Zhang[£], Daniel T. Chiu[‡], Changfeng Wu*[§], and Jason McNeill*[†]

[†]Department of Chemistry, Clemson University, Clemson, South Carolina 29634, United States
[‡]Department of Chemistry, University of Washington, Seattle, Washington 98195, United States
[§]Department of Biomedical Engineering, Southern University of Science and Technology, Shenzhen, Guangdong 518055, China
[£]Faculty of Health Science, University of Macau, Taipa 999078, Macau

TABLE OF CONTENTS

EXPERIMENTAL SECTION

Synthesis of Monomers and Polymers

3-Methyl-3-oxetanemethanol, 1,6-dibromohexane, 2,7-dibromofluorene, (4,4,5,5-tetramethyl-1,3,2-ioxaborolan-2-yl)benzene, bromobenzene, and chloroform-*d* were obtained from J&K Chemical Ltd. 9,9-Dioctyl-9*H*-fluorene-2,7-diboronic acid bis(pinacol) ester and 9,9-dioctyl-2,7-dibromofluorene were obtained from Derthon Optoelectronic Materials Science & Technology Co., Ltd.. Tetrabutyl ammonium bromide (Bu_4NBr) was purchased from Aladdin Chemistry Co., Ltd.. Poly-(styrene-*co*-maleic anhydride) (PSMA, MW = 1700), tetrakis-(triphenylphosphine) palladium(0) ($Pd[PPh_3]_4$, 99%), surfactant Triton X-100, dimethylsulfoxide, triarylsulfonium hexafluorophosphate salts, (3-Aminopropyl) trimethoxysilane (APS) and methyl-viologen dichloride were purchased from Sigma-Aldrich. The molecular weights of synthesized polymers were measured by the gel permeation chromatography (GPC) method (515HPLC pump, Waters, 2414 refractive index detector). ^{1}H NMR spectra were obtained on a 300 MHz Varian Mercury. ^{13}C NMR spectra were obtained on a 500 MHz Avance Bruker spectrometer.

Synthesis of 3-[(6-bromohexyloxy)methyl]-3-methyloxetane (**3**) is described as follows. 1, 6-dibromohexane (**2**; 35.9 g, 0.147 mol) was stirred in n-hexane (40 mL) with 3-methyl-3-oxetanemethanol (**1**; 5.0 g, 0.049 mol) and Bu_4NBr (0.2 g, 0.62 mmol), a solution of NaOH in deionized water (50 mL, 0.65 g/mL) was added and the mixture was stirred at r.t. for 24 h. After refluxed 2 hours, the mixture was washed with deionized water (200 mL), dried ($MgSO_4$) and the solvent was removed by rotary evaporation. The final product was obtained as a color less liquid after being purified by dry column chromatography on silica gel (ethyl acetate/n-hexane = 1/10 as eluent). Yield 10.1 g, 78%. ^{1}H NMR (300 MHz, $CDCl_3$, δ): 4.51 (d, 2H, J = 5.7 Hz), 4.35(d, 2H, J = 5.7 Hz), 3.47 (t, 2H, J = 6.4 Hz), 3.46 (s, 2H), 3.41 (t, 2H, J = 6.9 Hz), 1.91-1.82 (m, 2H), 1.65-1.56 (m, 2H), 1.51-1.35 (m, 4H), 1.31 (s, 3H). ^{13}C NMR (150 MHz, $CDCl_3$, δ): 79.93, 75.86, 71.11, 39.70, 33.59, 32.52, 29.16, 27.74, 25.15, 21.19.

Synthesis of 9, 9-di-{3-[(3-methyloxetan-3-yl)methoxy]hexyl)-2,7-dibromofluorene (**5**) is desribed as follows. 2,7-dibromofluorene (**4**; 1.3 g, 4 mmol) was dissolved in DMSO (35 mL) and stirred with Bu_4NBr (0.165 g, 0.51 mmol). NaOH (15 mL, 1.0 g/mL, in deionized water) was added slowly and the mixture was stirred at 60°C for 5 min. The compound 3-[(6-bromohexyloxy) methyl]-3-methyloxetane (**3**; 2.3 g, 8.8 mmol) in DMSO (15 mL) was added and the mixture was stirred. After refluxed 2 hours, the mixture was washed with deionized water (300 mL), dried ($MgSO_4$) and the solvent was removed by rotary evaporation. The final product was obtained as a colorless thick solid after being purified by dry column chromatography on silica gel (ethyl acetate/n-hexane =1/5 as eluent). Yield 2.2 g, 79%. mp: 63.2-64.0°C; ^{1}H NMR (300 MHz, $CDCl_3$, δ): 7.53-7.45(q, 6H), 4.45 (d, 4H, J = 5.7 Hz), 4.32(d, 4H, J = 5.7 Hz), 3.40 (s, 4H), 3.33 (t, 4H, J = 6.6 Hz), 1.94-1.88 (m, 4H), 1.43-1.34 (m, 4H), 1.26 (s, 6H), 1.15-1.05 (m, 8H), 0.63-0.50 (m, 4H); ^{13}C NMR (150 MHz, $CDCl_3$, δ): 152.33, 139.02, 130.18, 126.06, 121.45, 121.14, 80.16, 75.97, 71.43, 55.57, 40.08, 39.82, 29.60, 29.33, 25.68, 23.53, 21.33.

Synthesis of poly(9,9-dioctylfluorene) with side-chain oxetane terminus (do-PFO) is described as follows. In a 50 mL flask, 9,9-di-{3-[(3-methyloxetan-3-yl)methoxy]hexyl}-2,7-dibromofluorene (**5**) (346.3 mg, 0.5 mmol) and monomer 9,9-dioctyl-9*H*-fluorene-2,7-diboronic acid bis(pinacol) ester (**6**) (321.3 mg, 0.5 mmol) were dissolved in toluene (10 mL); Bu_4NBr (6.4 mg, 0.02 mmol) and Na_2CO_3 (6 mL, 2 M) were also added. The reactants were stirred at room temperature, and the flask was degassed and recharged with nitrogen (repeated 6 times) before and after addition of $Pd(PPh_3)_4$ (10 mg, 0.008 mmol) to the mixture. The mixed solution was stirred at 90 °C for 2 days under N_2 atmosphere, and then (4,4,5,5-tetramethyl-1,3,2-dioxaborolan-2-yl)benzene (30 mg) dissolved in toluene (1 mL) was introduced to remove bromine end groups. After 5 h, bromobenzene (0.3 mL) was added to remove boronic ester end groups and further stirred for 6 h. After the mixture was cooled to room temperature, it was poured into methanol (100 mL). The precipitated solid was filtered and washed by ammonia solution, deionized water, ethanol, and acetone. The crude products were dissolved in tetrahydrofuran (THF, 15 mL), filtered by using 0.22 μm membrane, and reprecipitated in methanol (100 mL). The precipitate was then redispersed in acetone (150 mL) and stirred for 24 h. The resulting polymer was collected by filtration, and then dried at 40 °C under vacuum for 2 days, finally resulting in pale yellowish green solid (374.0 mg, 81%). ^{1}H NMR (300 MHz, $CDCl_3$, δ): 7.96–7.80 (m, 4H), 7.77–7.52 (m, 8H), 4.46 (d, 4H, J = 5.7 Hz), 4.32 (d, 4H, J = 5.7 Hz), 3.40 (s, 4H), 3.34 (t, 4H, J = 6.6 Hz), 2.25–1.98 (m, 8H), 1.62–1.35 (m, 4H), 1.26 (s, 6H), 1.23–1.01 (m, 30H), 0.83 (m, 12H). Molecular weight was measured by GPC as Mn = 25 692, Mw = 64 360, PDI = 2.50.

Self-assembly and Characterization of Different Nanostructures

The conjugated polymer nanostructures were prepared by the modified reprecipitation method. First, conjugated polymer do-PFO was dissolved in THF to form a homogeneous solution at a concentration of 100 μg/mL. For preparation of anisotropic polymer nanostructures, various volumes (1 mL, 2mL, 4 mL) of do-PFO in THF solution were injected into 8 mL water containing 0.25 wt% Triton X-100 under sonication to yield ellipsoids, ellipsoid/nanowire mixture and nanowires, respectively. For preparation of spherical nanoparticles, 2 mL of do-PFO in THF solution were injected into 8 mL water under sonication. Finally, THF was evaporated by nitrogen (N_2) stripping under heating. The surfactant in the final solution can be readily removed by dialysis. UV−vis absorption spectra were recorded on a Shimadzu UV-2550 spectrophotometer. Fluorescence emission spectra were measured on a Hitachi F-4500 fluorometer. The particle diameter distributions and zeta potential of the nanoparticles were determined by dynamic light scattering with a Malvern Zetasizer Nano ZS instrument. The nanoparticle size and morphology were investigated by a Hitachi H-600 transmission electron microscope (TEM) and the high-resolution TEM images were obtained with a JEM-2100F electron microscope operating at 200 kV.

Polaron Tracking and Hyperspectral Superresolution Imaging

Superresolution imaging and polaron tracking were performed using a custom wide-field epifluorescence microscope described as follows. A 405 nm diode laser (50 mW) was used as the

excitation source. Inside the microscope (Nikon, TE2000-U), the excitation laser is reflected by a 410 nm long-pass dichroic mirror (Chroma) to a high numerical aperture objective (Nikon, Plan Apo TIRF, 100×, 1.45 NA, oil). The laser excitation at the sample focal plane exhibits a Gaussian profile with full width half maximum of ~20 μm. The typical excitation power at the center of the laser spot is estimated to be 35 W/cm^2. Single particle fluorescence was collected by the objective lens, filtered through a 410 nm long-pass filter and then focused onto a sCMOS camera (Hamamatsu, Orca flash 4.0) by a tube lens, yielding a pixel pitch of 110 nm/pixel. The typical detector settings were gain of 0.5, rolling shutter mode. The experimental camera gain factor is 0.52 electrons per count, as determined by analysis of photon counting noise for a flat field. For measurement of single-particle fluorescence spectra, a transmission grating with 300 grooves per mm (Thorlabs, GT25-03) was placed in front of the sCMOS camera to disperse single particle emission. A dispersion factor of 0.55 nm per pixel was determined using a 500 ± 10 nm band pass filter. Based on the single-particle fluorescence spot width (PSF) of roughly 4–5 pixels (FWHM), which roughly corresponds to the slit width of the spectrometer, the spectroscopic resolution is roughly 2.5 nm.

PFO nanowires were mixed with fluorescent beads and immobilized on APS functionalized glass surface, inside an imaging chip (ibidi μ-slide). The sample was kept under N_2 protection during the entire experiment. A motorized stage (ASI, MS-2000) was used to move the sample. For polaron tracking, over 200000 frames of fluorescence microscopy images were acquired at a framerate of 1 kHz. For nanowire segments that exhibited two-level fluorescence blinking, the images acquired during the fluorescence "off" states were subtracted frame-by-frame from the image of the adjacent fluorescence "on" state to recover the quenched point-spread-function (PSF).[1] A custom Matlab script (Mathworks) was employed to analyze the subtracted images. The positions of the polaron were roughly located by searching for pixels above the threshold frame by frame and comparing their intensities to the adjacent pixel. The precise position of the polaron was then determined by nonlinear least-squares fitting of a Gaussian function to the PSFs. Typically 7×7 pixels were used for the fitting (3 pixels on each side of the central pixel). Prior to superresolution imaging, water solution of methyl-viologen dichloride (500 nM) was injected into the imaging chip. Then, over 20000 frames of fluorescence microscopy images were acquired at a framerate of 50 Hz. As methyl-viologen cations (MV^{2+}) adsorbed onto the nanowire, the conjugated polymer emission was gradually quenched. Occasional fluorescence recovery can be observed when a quencher unbound from the surface. Change point analysis was employed to locate individual quenching/recovery events. The single-step quenching depth and transition rates determined were then plugged into a hidden-Markov model to perform a refined search of transition steps. For transitions that involved a single quencher, difference images were obtained by comparing the fluorescence images before and after the transition. In the (absolute) difference images, Gaussian-shaped PSF of local emitters can be observed at the n = 0 spot while a long stripe, which corresponds to the local fluorescence spectra, can be observed at the n = 1 spot. The precise position of the emitters was determined from the n=0 spot using the 2D Gaussian fitting procedures described above. The script then checked the number of peaks identified and FWHM obtained

from the fitting to rule out the possibility of simultaneous adsorption of multiple quenchers. The bright stripe was summed along the Y axis (10 pixels in total) to obtain the emission spectrum. The positions of fluorescent beads were tracked during the experiments to perform drift correction and align hole polaron trajectories with the superresolution images.

SUPPORTING RESULTS AND DISCUSSION

Synthesis of do-PFO Polymer

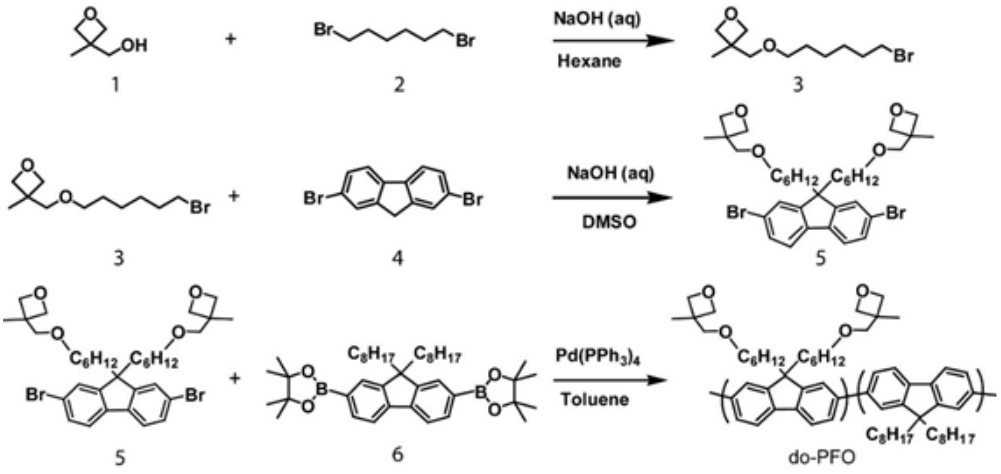

Figure. S1 Synthesis of do-PFO Polymer.

Evolution of Morphology

PFO nanowires were synthesized using a novel self-assembly method. We discovered that nano-precipitation of do-PFO resulted in self-assembly of a variety of nanostructures. By adding a small amount of Triton X-100 in the water solution (0.25 wt%) and varying injection volume of do-PFO in THF, anisotropic nanostructures such as ellipsoids and nanowires can be obtained (Figure S2). Without the oxetane terminus, only spherical structures were obtained, indicating the critical role of the terminus groups. TEM images of different morphologies were provided in the main text. As the morphology evolves from spheres to wires, the β phase content in the nano-assembly increases, as indicated by the red-shifted highest absorption peak (403 nm) and the increasing shoulder peak (436 nm), which are consistent with the β phase 0-0 and 0-1 transitions (Figure S3a).[2-3] The nanowires exhibited significantly higher fluorescence quantum yield and increased 0-0/0-1 peak intensity ratio, as compared to nanoparticles and nanorods (Figure S3b). These observations are likely a result of strong intra-chain coupling in the PFO nanowires, which reduces the formation of weakly-emissive inter-chain species and favors intra-chain excitation with J-type characteristics.[4-5]

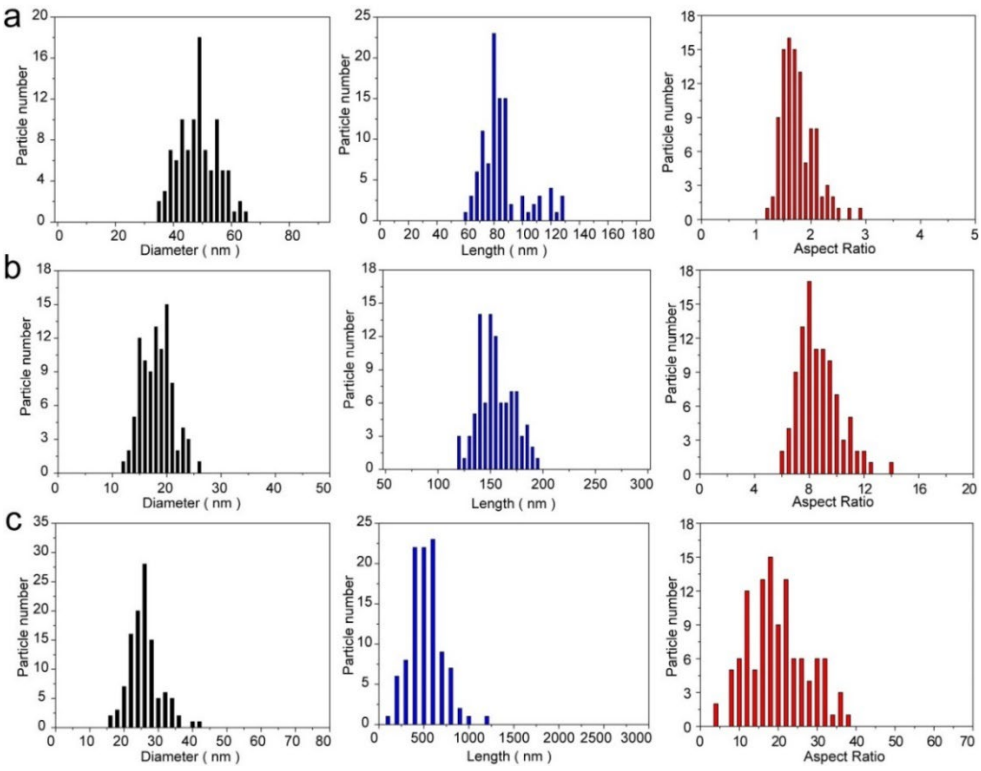

Figure. S2 Statistical analysis on the diameter, length and aspect ratio of the do-PFO nanostructures by analyzing a number of TEM images, showing the evolution from elliposoid (a) to elliposoid/nanowire mixture (b), then to nanowires (c).

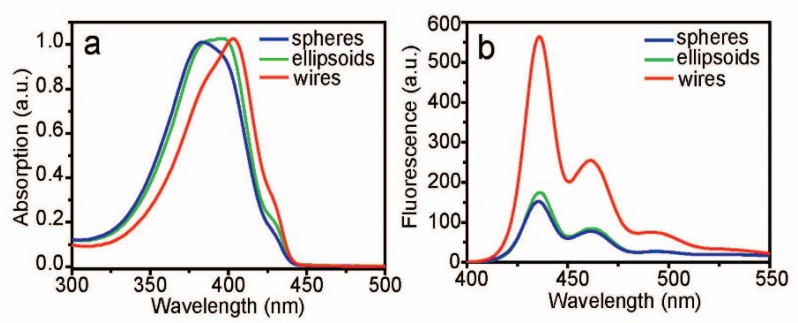

Figure. S3 (a) Absorption spectra of different do-PFO nano-assemblies: spheres (blue), ellipsoids (green) and wires (red). (b) Emission spectra of different do-PFO nano-assemblies: spheres (blue), ellipsoids (green) and wires (red).

Identification of the Quencher Species

In conjugated polymer systems, exciton quenching by hole polarons has been extensively studied.[6-9] Hole polarons in many conjugated polymers are essentially non-fluorescent and possess red-shifted absorption spectra as compared to neutral polymers,[9-10] which makes energy transfer from

excitons to hole polarons an efficient pathway for non-radiative decay. In conjugated polymer based light-emitting devices, fluorescence quenching by charge carriers is an important loss mechanism, which results in decrease in device efficiency at high current density.[11-12] Early single-molecule studies of conjugated polymers showed that conjugated polymers exhibited discrete intensity jumps on the millisecond to second scale,[13-14] which is too slow for the triplet state dynamics (microsecond scale).[15] The generation rate of the quencher species was excitation power dependent and sensitive to the presence of molecular oxygen.[13-14] Single-molecule electrochemical studies of conjugated polymers showed that injection and extraction of holes can result in similar fluorescence intensity modulation and the injected hole polaron can be stored for an extended period of time.[8, 16] Considering the reversibility of the electron transfer reaction, the lifetime of the quenched state, and the similarity in the modulation depth, it was concluded that the slow, discrete fluorescence blinking of conjugated polymer is likely caused by generation and depletion of hole radicals. [7, 16] In air, hole polaron formation is facilitated by the electron-transfer from conjugated polymer excited states to molecular oxygen,[14] whereas in inert environment, hole generation is typically less efficient, possible reaction pathways include, electron transfer to substrate, charge separation at grain boundary, etc.[17] In PFO nanowires, we also observed excitation power dependent blinking behavior (Figure S4), similar to the previously reported photoblinking dynamics associated with generation and depletion of hole polarons. We analyzed the fluorescence blinking trajectories with autocorrelation and fitted the autocorrelation curves to bi-exponential functions. According to the previous studies,[15, 18] the autocorrelation time constants on the second scale correspond to the slow, discrete blinking dynamics of conjugated polymers. Under 35, 70, 140 W/cm^2, the averaged photoblinking time constants are 2.97, 1.81, and 1.05 s, respectively (table S1), which indicates that the quenchers are photo-generated and are unlikely to be non-fluorescent aggregate species, such as H-aggregate. Aggregate species in conjugated polymers are also unlikely to exhibit such high mobilities as we observed experimentally. In addition, the lifetime of the quencher species is much too long for conjugated polymer triplet state. Overall, considering all the observations, we concluded that the quenchers that we studied are likely hole polarons, rather than other species.

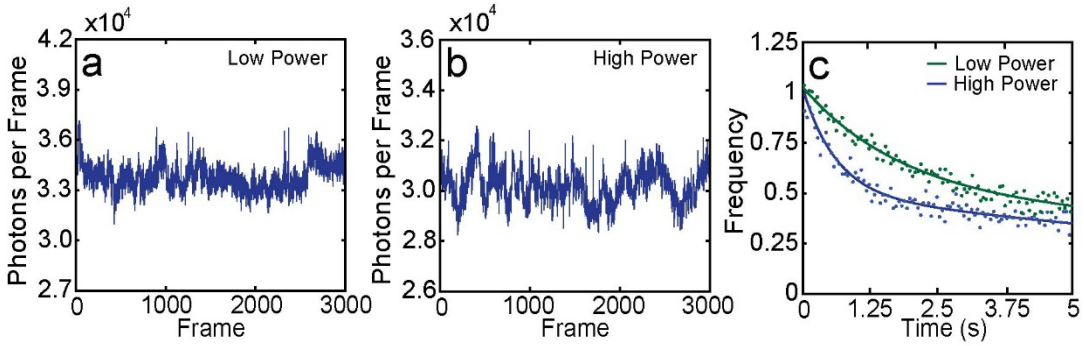

Figure. S4 (a) A representative fluorescence trajectory of PFO nanowires, acquired under 35 W/cm^2 excitation power density, 50 Hz framerate. (b) A representative fluorescence trajectory of PFO nanowires, acquired under 140 W/cm^2 excitation power density, 50 Hz framerate. (c) Representative autocorrelation

traces of the fluorescence intensity trajectories acquired under 35 W/cm^2 (green) and 140 W/cm^2 (blue), both fitted to bi-exponential functions. For 35 W/cm^2, τ_1=0.13 s, τ_2=2.21 s. For 140 W/cm^2, τ_1=0.09 s, τ_2=0.81 s.

Table S1. Time constants obtained from the intensity autocorrelation analysis

	35W/cm^2	70W/cm^2	140W/cm^2
τ_1	$2.97 \pm 1.91s$	$1.81 \pm 1.77\ s$	$1.05 \pm 1.18\ s$
τ_2	$0.21 \pm 0.17\ s$	$0.17 \pm 0.20\ s$	$0.18 \pm 0.16\ s$

Determination of Localization Uncertainties

The localization uncertainty of conventional localization microscopy is related to shot noise and the optical characteristics of the imaging system, which is given by[19]

$$\sigma = \sqrt{\frac{s^2}{N} + \frac{\alpha^2/12}{N} + \frac{8\pi s^4 b^2}{\alpha^2 N^2}}, \quad (1)$$

where s is the standard deviation (std) of the PSF, α is the pixel size, N is the number of photons used for localization fitting, b is the background noise, which has contributions from readout noise, autofluorescence, and scattered light. In our system, the std of the typical single molecule PSF is ~130 nm, the pixel size is 110 nm, the background noise under the typical imaging condition is 5–10. When N >1500, the second and third terms are small (<10%) compared to the first term that the equation 1 can be simplified to $\sigma = s/\sqrt{N}$, which is the PSF size s divided by the signal-to-noise ratio (SNR) of the image $N/\sqrt{N} = \sqrt{N}$.

In bleaching/blinking-assisted localization microscopy, the noise of the subtracted image is mainly dictated by shot noise of the background fluorophores in the original images. The shot noise contributions from each image n_1 (before quenching) and n_2 (after quenching) are given by[20]

$$n_i = \frac{\sqrt{N_i}}{\sqrt{F_i}}, \quad (2)$$

where N_i is the number of photons from background fluorophores in a diffraction-limited spot, and F_i is the number of averaged frames for each state. Since the shot noise in the before and after images should have no correlation, according to the principle of error propagation, the SNR of the subtracted image is given by $(N_1 - N_2)/\sqrt{n_1^2 + n_2^2}$. The equation 1 can then be written as

$$\sigma = \frac{s\sqrt{n_1^2 + n_2^2}}{N_1 - N_2}. \quad (3)$$

As indicated by the equation 1 and the equation 3, when $N_1 - N_2$ photons were used for localization, the localization error of bleaching/blinking-assisted localization microscopy is $\sqrt{(n_1^2 + n_2^2)}/\sqrt{N_1 - N_2}$ times higher the conventional localization microscopy. This ratio can be referred to as the subtraction penalty factor. In superresolution mapping, we observed that the penalty factor decreased with the background fluorophore intensity. Eventually, when the local emission was completely quenched ($N_2 = n_2 = 0$), the penalty factor reached 1, indicating that, under this condition, subtraction did not introduce additional error as compared to direct localization, which will be discussed in detail below.

Using equation 3, we calculated the theoretical localization uncertainties for polaron tracking and superresolution mapping. By analyzing 1D slices of the nanowire PSF before and after a quenching event, we determined that, for an unquenched nanowire, a hole polaron or MV^{2+} can quench 18-32% or 15-25% of the local emission, respectively (Figure S5a). The number of photons for localization $N_1 - N_2$ was calculated by summing the PSF in the subtracted image. To estimate the number of background photons in a diffraction-limited area of unquenched nanowires (N_1), we fitted the recovered PSF in the subtracted image to a 2D Gaussian function, scaled it to the same peak intensity as the 1D unquenched nanowire PSF, and then performed integration. The background photons of the quenched nanowire N_2 was then calculated by the intensity difference. The analysis results were summarized in table S2. For polaron tracking, 10 frames were averaged before the transition to generate an "on" state average, and then "off" state images were subtracted frame-by-frame from the "on" state average image, where as for superresolution mapping, 3 frames were averaged for both "on" and "off" states before the subtraction. In both cases, the std of the recovered PSF is ~130 nm. According to table S2, for 1 kHz polaron tracking, $1.9\pm0.4\times10^3$ photons were used for localization. For conventional localization microscopy, this yields a localization uncertainty of 3.3-4.4 nm. However, the typical background fluorophore photon counts N_1 and N_2 in the original images were $8.7\pm2.2\times10^3$ and $6.8\pm2.2\times10^3$, respectively, which yielded a penalty factor of 1.7-2.5. Overall, we determined that the uncertainty for 1 kHz polaron tracking ranged from 5.6 to 11 nm. For superresolution mapping, typically $2.2\pm0.6\times10^3$ photons were used for localization, which should yield a localization uncertainty of 2.7-3.6 nm for conventional localization microscopy. The penalty factor decreased from 1.5-2.5 to ~1, as the nanowires intensity decreased from maximum to 0. As a result, localization uncertainties of 5.2-9.0 nm and 2.7-3.6 nm were obtained at the highest and lowest background fluorophore intensities. The theoretical uncertainty was further validated experimentally by analyzing localization clusters in the superresolution mapping. For adjacent long-lived steps in the intensity decay, sufficient number of localization points can be accumulated to provide a localization histogram. As shown in Figure S5b, for the same nanowire, the experimental localization uncertainties (std of the histogram) at the highest and lowest background fluorophore intensities were 10.1 and 4.0 nm, respectively, which are consistent with the theoretical localization uncertainties calculated from the equation 3 (9.0 and 3.5 nm). Minimal binning in the initial localization ensured enough data points for downstream autocorrelation and mean square displacement (MSD) analysis. When constructing the superresolution map, the localization uncertainties can be convenient reduced by

binning the localization points of the same states, which is equivalent to binning multiple frames in the localization analysis. As shown in Figure S5c, 4-point binning resulted in ~2 times improvement in the localization precision, which is consistent with the prediction of the equation 3.

Table S2. Parameters for Theoretical Localization Uncertainty Calculation

	Number of photons for localization N_1- N_2	Number of background photons from a unquenched nanowire N_1	Number of background photons from a quenched nanowire N_2
1 kHz polaron tracking	$1.9\pm0.4\times10^3$	$8.7\pm2.2\times10^3$	$6.8\pm2.2\times10^3$
50 Hz superresolution mapping	$2.2\pm0.6\times10^3$	$9.6\pm2.6\times10^3$	$7.4\pm2.5\times10^3$

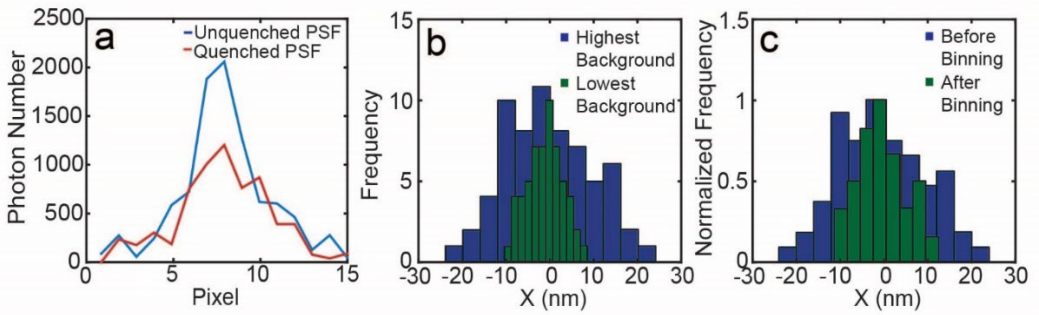

Figure. S5 (a) 1D slices of the nanowire PSF before (blue) and after a quenching event (red). 3 frames of images were averaged for each state. (b) Localization histograms obtained at the highest (blue) and lowest (green) background fluorophore intensities. (c) Localization histograms before (blue) and after 4-point binning (green).

Recognizing Quenching/Recovery Steps

As MV^{2+} adsorbed onto the nanowire, the conjugated polymer emission was gradually quenched. Occasional fluorescence recovery can be observed when a quencher unbound from the surface. Change point analysis was employed to locate individual quenching/recovery steps and estimate average "on"/"off" transition rates (Figure S6a).[21] Intensity histogram was used to estimate single-step quenching depths and total number of quenchers adsorbed over time (Figure S6b). These parameters were plugged into a previously reported hidden-Markov model to perform a refined search of the underlying transitions, which is briefly described as follows.[22-23] Based on the total number of quenchers adsorbed N, the intensity trajectory was divided into N state. To account for variations in quenching depth of each step, the intensity of each state was assumed to follow a Gaussian probability distribution with std equals to the std of the quenching depth distribution. To account for Poisson noise, we generated a Poisson distribution at each possible intensity of the state and weighted it by the probability of the Gaussian distribution. For each state, the overall

intensity probability distribution was given by the sum of all the Poisson distributions. For a given frame, the probability of the nanowire to be in each state was calculated by plugging the fluorescence intensity into the N probability distributions to generate an array. For a total number of M frames, we obtained an $N \times M$ probability matrix, indicating $N \times M$ transition pathways. When linking different states between adjacent frames, the probability of the corresponding pathway was multiplied by the "on" or "off" transition probability (Figure S7). For all the pathways, the one with the highest overall probability was used to recover the underlying transition steps of the intensity trajectory (Figure S6c). It should be noted that the transition probability likely varied from step to step, depending on the local environment. However, since most of the false positive transitions were caused by shot noise and were on a very different timescale (typically one bin in the intensity trace) than real transitions, there is a range of transition rates that can yield comparable results for the hidden-Markov model. Typically, the averaged transition rate was used as it provided most consistent performance. For single-step transitions recognized by the model, difference images were obtained by comparing the fluorescence images before and after the transition, which was used to extract the positions and spectra of the emitters. Overall, suppressing of the shot-noise-induced false positives yielded cleaner superresolution images with less localization errors. By averaging over all the frames in each step, the adsorption position of each quencher during the intensity decay can be determined with high precision. As shown in Figure S8, the localized quenchers were dispersed on the nanowire with the nearest neighbor distance of ~19 nm, consistent with the expected density of quenchers. It is possible that there was a small fraction of quenchers that were located close to each other (<5 nm). In such cases, only the first adsorbed quencher was localized, as the following adsorption events did not cause pronounced intensity changes. In addition, since these quenchers were in close proximity, neglecting the following events should not affect the quality of the superresolution map.

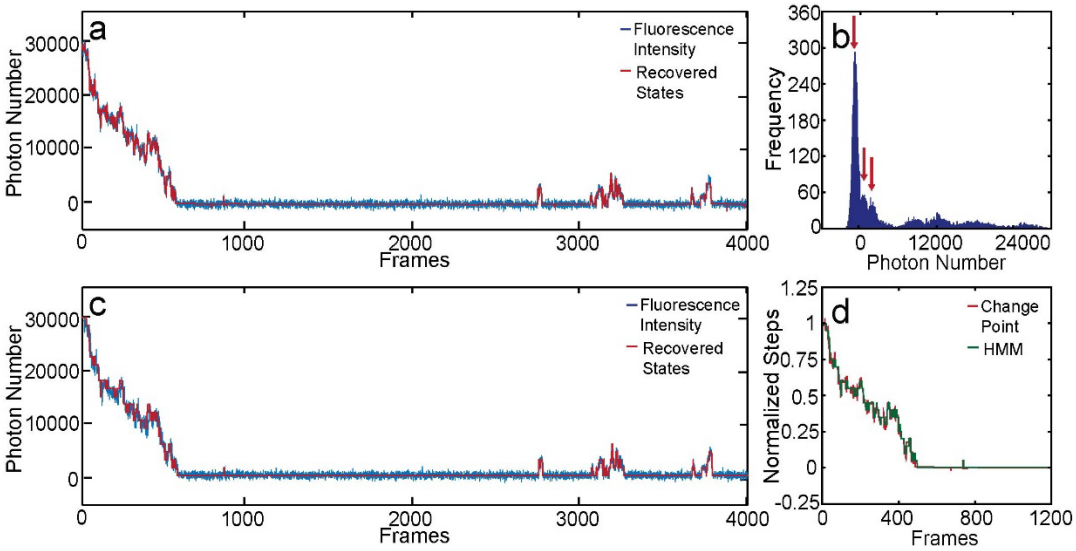

Figure. S6 (a) Fluorescence intensity trajectory of a PFO nanowire, showing binding and unbinding dynamics of quenchers. Steps recognized by the change point analysis were plotted in red. (b) Fluorescence

intensity histograms of the trajectory shown in panel a. The clusters highlighted by the red arrows indicate states separated by single-step transitions. (c) Fluorescence intensity trajectory shown in panel a (blue), overlaid with steps recognized by the hidden-Markov model (red). (d) Comparisons of steps recovered by the change point analysis (red) and the hidden-Markov model (green).

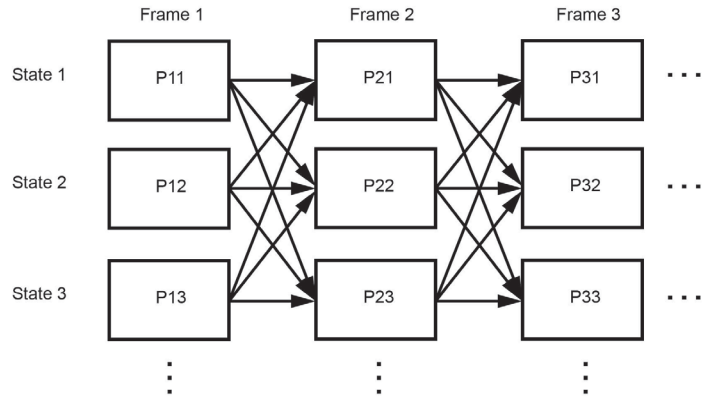

Figure. S7 Principle of the hidden-Markov model.

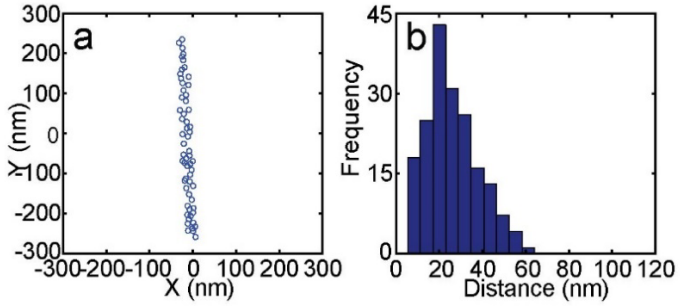

Figure. S8 (a) Averaged positions of the quenchers adsorbed during the intensity decay. (b) Distribution of the distances to the nearest neighbour, obtained from the analysis of multiple nanowires.

Analysis of Hole Polaron Hopping Dynamics Resolved by the Two Methods

Here, we compared the polaron tracking results obtained using two different methods. In the first method, polaron tracking and structural mapping were performed without MV^{2+} (Figure S9a). As polaron moved along the nanowire, different areas were quenched, which allowed mapping of emission sites through correlated single particle spectrum analysis.[24] Due to limited photon number, the polaron tracking framerate was set to 50 Hz. In the second method, polaron tracking and superresolution mapping were performed separately (Figure S9b). The polaron tracking was performed at 1000 Hz framerate, whereas the superresolution mapping was performed at 50 Hz framerate, utilizing binding and unbinding dynamics of MV^{2+}. We analyzed the hole polaron trajectories acquired at 50 and 1000 Hz using MSD and autocorrelation (Figure S9c, d). The MSDs of the 1000 Hz hole polaron trajectories showed clear two-step behavior with steep increase at the

early time and slower continues increase on the longer timescales, which correspond to rapid hole transport within the β phases and slower inter-domain hopping dynamics, respectively. In contrast, the MSDs of the 50 Hz hole polaron trajectories showed no steep early increase. Early time MSD fitting yielded hole mobilities of 10^{-8}-10^{-7} cm^2/Vs and 10^{-7}-10^{-6} cm^2/Vs for the 50 Hz and 1000 Hz trajectories, respectively (Figure S9e). Similarly, the autocorrelation of the 50 and 1000 Hz trajectories also showed very different behavior at early time. Early time autocorrelation fitting yielded time constants of 40-150 ms and 2-40 ms for the 50 Hz and 1000 Hz trajectories, respectively (Figure S9f). These results suggested that the fast polaron motion in the β phase were not completely resolved at 50 Hz framerate.

While the temporal resolution is lower, the simultaneous tracking and mapping approach has a unique advantage as it can monitor interfacial hopping through correlated spectrum changes and directly measure hopping rates (Figure S9a). In the two-step approach, measurement of interfacial hopping rate requires locating grain boundaries through superresolution mapping. It should be noted that, near grain boundary, the local emission sometimes has contributions from both sides. Across the grain boundary, there is usually a transition point, where the major contributor of the local emission changes from one side to the other. Since we colored the superresolution map according to the local emission peak wavelength, this transition results in change of color on the superresolution map, which were used to approximately locate the grain boundaries.

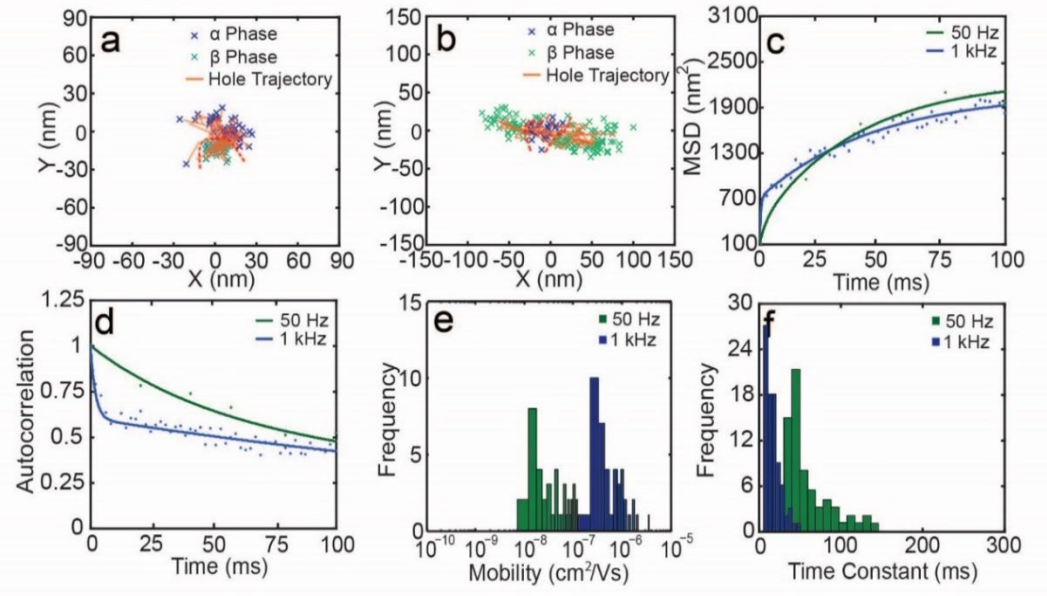

Figure. S9 (a) A hole polaron trajectory obtained from the simultaneous tracking and mapping approach, under 50 Hz framerate. The grain boundary is indicated by the red dashed line. (b) A hole polaron trajectoy obtained under 1 kHz framerate, overlaid with the superresolution spectral map. The grain boundaries are indicated by the red dashed lines. (c) Representative MSDs of trajectories acquired under 50 (green) and 1000 Hz (blue) framerate, both fitted a bi-exponential confined diffusion function. For 50 Hz MSD, D_{f1}=4.1×10^4 nm^2/s, L_{f1}=15 nm, D_{f2}=2.1×10^4 nm^2/s, L_{f2}=41 nm. For 1000 Hz MSD, D_{f1}=5.4×10^5 nm^2/s, L_{f1}=23 nm, D_{f2}=1.3×10^4 nm^2/s, L_{f2}=35 nm. (d) Representative autocorrelation of trajectories acquired

under 50 (green) and 1000 Hz (blue) framerate, both fitted a bi-exponential decay function. For 50 Hz autocorrelation, τ_1=0.05 s, τ_2=0.35 s. For 1000 Hz MSD, τ_1=0.003 s, τ_2=0.28 s. (e) Hole mobilities obtained from the fitting of early time MSD of the 50 (green) and 1000 Hz (blue) trajectories. (f) Time constants obtained from the fitting of early time autocorrelation of the 50 (green) and 1000 Hz (blue) trajectories.

Modulation of Single Nanowire Emission by Excitation Polarization

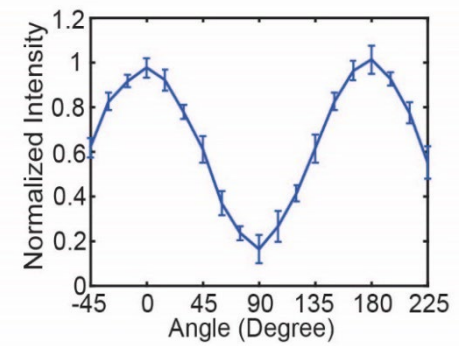

Figure. S10 Single nanowire emission intensity plotted versus the angle between excitation polarization and the nanowire longitudinal axis. The curve represents an average of 25 nanowires.

Change Transport Parameter Distributions

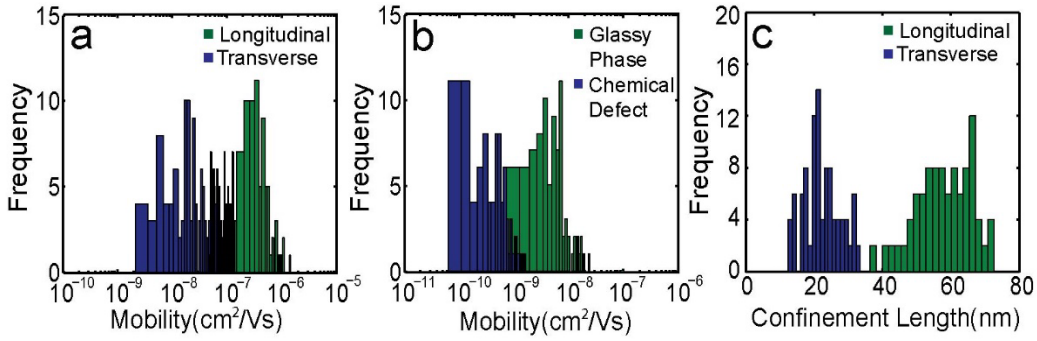

Figure. S11 (a) Hole mobility distributions for longitudinal (green) and transverse (blue) transport in the β phase. (b) Hole mobility distributions obtained from trajectory segments showing disorder (green) and defect (blue) trapping. (c) Confinement length distributions for longitudinal (green) and transverse (blue) transport in the β phase.

Determination of the Hole Polaron Trap Depth

As indicated by the MSD analysis, a variety of dynamics could be observed for hole polarons near the grain boundaries, including rapid diffusion in the β phase as well as trapped motion associated with the α phase. In addition, depending on the contact area of the two phases, there could be a variety of sites involved in the trapping dynamics. As described previously, the complexity of the data analysis can be greatly reduced by dividing the interfacial trajectories into segments and performing change point as well as autocorrelation/MSD analysis with each segment.[18] In some segments, we observed single-exponential dynamics likely associated with single-step trapping, i.e., the position autocorrelation fits well to a single exponential decay and the MSD fits well to a single-exponential confined diffusion function (Figure S12a-c). As shown in Figure S12d, the localization histogram of the segment revealed a major cluster, which corresponds to a trap site, and a small cluster, which corresponds to a shallower site. Based on the spatial extent of the trap in the localization histogram, we adjusted the threshold in the change point analysis to determine polaron escape frequency and single-step hopping distances. The averaged trapping time and hopping distances determined were typically close to the values of the autocorrelation time constant and MSD confinement length (Figure S12e, f). The hopping distances determined along the X and Y axes were used to calculate the 2D hopping distance ($r_{2D}^2 = r_x^2 + r_y^2$). To determine the barrier height, the averaged polaron trapping time and single-step hopping distance determined from the change point analysis were plugged in to the Miller-Abrahams equation, which is given by,

$$k_{ET} = v_0 e^{-2\gamma r_{2D}} e^{-\frac{\Delta E}{kT}}, \quad (4)$$

where k_{ET} is the hopping rate, r_{2D} is the 2D hopping distance, ΔE is the energy barrier height, v_0 is the attempting rate, γ is the inverse localization radius.[25] According to the previous literature values,[26] v_0=10^{11} s^{-1} and γ=1 $Å^{-1}$ were used for our calculation. While the example above corresponds to disorder trapping, similar strategy can be used to analyze polaron hopping dynamics associated with chemical defects.

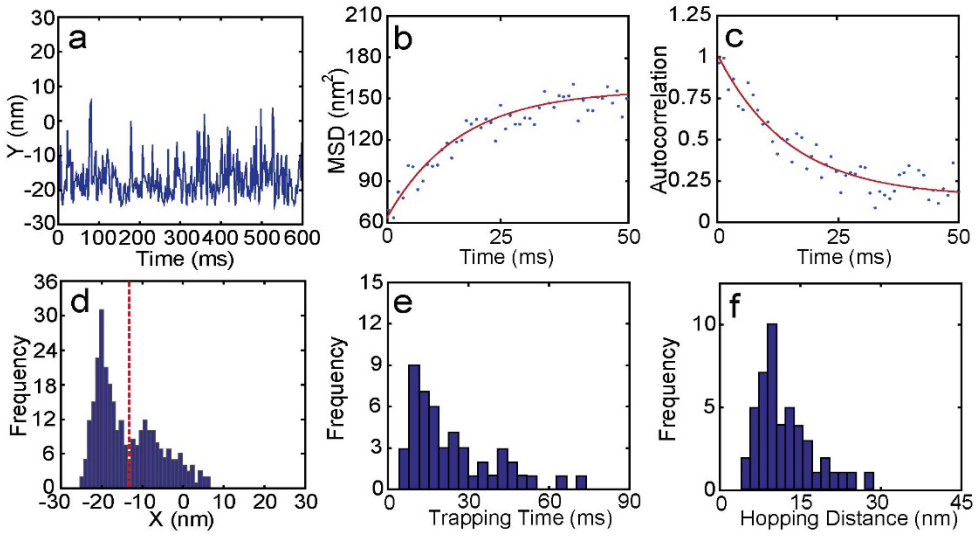

Figure. S12 (a) A representative trajectory segment showing hopping dynamics of a hole polaron. (b) MSD of the segment, fitted to a single-exponential confined diffusion function, D_f=6.2×10^3 nm^2/s, L_f=8.9 nm. (c) Autocorrelation trace of the segment, fitted to a single-exponential decay, τ=15 ms. (d) Localization histogram of the segment. The dashed line qualitatively indicates the boundary between the sites. (e) The trapping time and (f) the single-step hopping distance of the hole polaron, determined from the change point analysis.

REFERENCES

1. Burnette, D. T.; Sengupta, P.; Dai, Y.; Lippincott-Schwartz, J.; Kachar, B., Bleaching/blinking assisted localization microscopy for superresolution imaging using standard fluorescent molecules. *Proc. Natl. Acad. Sci. U. S. A.* **2011,** *108* (52), 21081-21086.
2. Scherf, U.; List, E. J., Semiconducting polyfluorenes—towards reliable structure–property relationships. *Adv. Mater.* **2002,** *14* (7), 477-487.
3. Prins, P.; Grozema, F. C.; Nehls, B. S.; Farrell, T.; Scherf, U.; Siebbeles, L. D., Enhanced charge-carrier mobility in β-phase polyfluorene. *Phys. Rev. B* **2006,** *74* (11), 113203.
4. Spano, F. C.; Silva, C., H-and J-aggregate behavior in polymeric semiconductors. *Annu. Rev. Phys. Chem.* **2014,** *65*, 477-500.
5. Niles, E. T.; Roehling, J. D.; Yamagata, H.; Wise, A. J.; Spano, F. C.; Moulé, A. J.; Grey, J. K., J-aggregate behavior in poly-3-hexylthiophene nanofibers. *J. Phys. Chem. Lett.* **2012,** *3* (2), 259-263.
6. Yu, J.; Song, N. W.; McNeill, J. D.; Barbara, P. F., Efficient exciton quenching by hole polarons in the conjugated polymer MEH-PPV. *Isr. J. Chem.* **2004,** *44* (1-3), 127-132.
7. Gesquiere, A. J.; Park, S.-J.; Barbara, P. F., Hole-induced quenching of triplet and singlet excitons in conjugated polymers. *J. Am. Chem. Soc.* **2005,** *127* (26), 9556-9560.
8. Bolinger, J. C.; Traub, M. C.; Adachi, T.; Barbara, P. F., Ultralong-range polaron-induced quenching of excitons in isolated conjugated polymers. *Science* **2011,** *331* (6017), 565-567.
9. Montilla, F.; Ruseckas, A.; Samuel, I. D., Exciton–Polaron Interactions in Polyfluorene Films with β-Phase. *J. Phys. Chem. C* **2018,** *122* (18), 9766-9772.
10. Wiebeler, C.; Tautz, R.; Feldmann, J.; Von Hauff, E.; Da Como, E.; Schumacher, S., Spectral signatures of polarons in conjugated co-polymers. *J. Phys. Chem. B* **2013,** *117* (16), 4454-4460.
11. Scholz, S.; Kondakov, D.; Lussem, B.; Leo, K., Degradation mechanisms and reactions in organic light-emitting devices. *Chem. Rev.* **2015,** *115* (16), 8449-8503.
12. Giebink, N. C.; Forrest, S., Quantum efficiency roll-off at high brightness in fluorescent and phosphorescent organic light emitting diodes. *Phys. Rev. B* **2008,** *77* (23), 235215.
13. Vanden Bout, D. A.; Yip, W.-T.; Hu, D.; Fu, D.-K.; Swager, T. M.; Barbara, P. F., Discrete intensity jumps and intramolecular electronic energy transfer in the spectroscopy of single conjugated polymer molecules. *Science* **1997,** *277* (5329), 1074-1077.
14. Yu, J.; Hu, D.; Barbara, P. F., Unmasking electronic energy transfer of conjugated polymers by suppression of O2 quenching. *Science* **2000,** *289* (5483), 1327-1330.
15. Yip, W.-T.; Hu, D.; Yu, J.; Vanden Bout, D. A.; Barbara, P. F., Classifying the photophysical dynamics of single-and multiple-chromophoric molecules by single molecule spectroscopy. *J. Phys. Chem. A* **1998,** *102* (39), 7564-7575.
16. Palacios, R. E.; Fan, F.-R. F.; Grey, J. K.; Suk, J.; Bard, A. J.; Barbara, P. F., Charging and discharging of single conjugated-polymer nanoparticles. *Nat. Mater.* **2007,** *6* (9), 680-685.
17. Reid, O. G.; Pensack, R. D.; Song, Y.; Scholes, G. D.; Rumbles, G., Charge photogeneration in neat conjugated polymers. *Chem. Mater.* **2013,** *26* (1), 561-575.
18. Jiang, Y.; Nongnual, T.; Groff, L.; McNeill, J., Nanoscopy of single charge carrier jumps in a conjugated polymer nanoparticle. *J. Phys. Chem. C* **2018,** *122* (2), 1376-1383.

19. Thompson, R. E.; Larson, D. R.; Webb, W. W., Precise nanometer localization analysis for individual fluorescent probes. *Biophys. J.* **2002,** *82* (5), 2775-2783.
20. Simonson, P. D.; Rothenberg, E.; Selvin, P. R., Single-molecule-based super-resolution images in the presence of multiple fluorophores. *Nano Lett.* **2011,** *11* (11), 5090-5096.
21. Chen, K.; Wang, B.; Guan, J.; Granick, S., Diagnosing heterogeneous dynamics in single-molecule/particle trajectories with multiscale wavelets. *ACS Nano* **2013,** *7* (10), 8634-8644.
22. McKinney, S. A.; Joo, C.; Ha, T., Analysis of single-molecule FRET trajectories using hidden Markov modeling. *Biophys. J.* **2006,** *91* (5), 1941-1951.
23. Joo, C.; Balci, H.; Ishitsuka, Y.; Buranachai, C.; Ha, T., Advances in single-molecule fluorescence methods for molecular biology. *Annu. Rev. Biochem.* **2008,** *77*, 51-76.
24. Jiang, Y.; McNeill, J., Superresolution mapping of energy landscape for single charge carriers in plastic semiconductors. *Nat. Commun.* **2018,** *9* (1), 4314.
25. Miller, A.; Abrahams, E., Impurity conduction at low concentrations. *Phys. Rev.* **1960,** *120* (3), 745.
26. Tessler, N.; Preezant, Y.; Rappaport, N.; Roichman, Y., Charge transport in disordered organic materials and its relevance to thin-film devices: a tutorial review. *Adv. Mater.* **2009,** *21* (27), 2741-2761.